Fe²⁺/Fe³⁺ substitution in hydroxyapatite: Theory and experiment

Ming Jiang,[1,2] J. Terra,[3] A. M. Rossi,[3] M. A. Morales,[3] E. M. Baggio Saitovitch,[3] and D. E. Ellis[1]

[1]*Department of Physics and Astronomy and Materials Research Center, Northwestern University, Evanston, Illinois 60208*
[2]*Department of Physics, Yantai University, Yantai, People's Republic of China, 264005*
[3]*Centro Brasileiro de Pesquisas Fisicas, Rio de Janeiro, Brazil, 22290*

Electron paramagnetic resonance, Mössbauer spectroscopy, and electronic structure calculations were combined in order to study the local geometry of Fe^{2+}/Fe^{3+} in Fe-doped hydroxyapatite. Atomistic simulations were carried out to obtain estimates of local geometry and lattice strain associated with fourfold, fivefold, and sixfold Fe sites. First-principles embedded cluster density functional calculations were performed to investigate the electronic structure associated with the substitution of calcium by Fe^{2+}/Fe^{3+}. Mössbauer isomer shift, quadrupole splitting, and the hyperfine magnetic field were calculated for each site and local coordination, for comparison to an experimental fit to a five-line model consisting of two bulk sites each for Fe^{2+} and Fe^{3+} and a surface hematitelike Fe^{3+} species.

I. INTRODUCTION

Hydroxyapatite (HAP), $Ca_{10}(PO_4)_6(OH)_2$, which is the basic mineral component of hard tissues (bone, teeth) has been extensively studied and used as a replacement material in medicine and dentistry.[1] In addition to its application as a bioceramic material, it is proposed as an environmental adsorvent of metal ions due to its cation-exchange property.[2]

The incorporation of impurites, via either ionic exchange or diffusion, affects morphology, solubility, lattice parameters, and consequently the stability of the material. The material, biological, and chemical properties are intimately related with the variation in the electronic structure caused by defects and impurities. Thus it is necessary to understand the relationship between structural aspects and the material properties upon impurity incorporation.

Recent work from this group has combined theory and experiments to predict the most favorable location and geometry for CO_2^- radicals in *A*-type carbonated HAP, which was studied by IR, electronic paramagnetic resonance (EPR), and electron-nuclear double resonance (ENDOR) spectroscopies.[3] The basic bonding and structural characteristics of ideal crystalline HAP show that there are two different calcium sites Ca(1) and Ca(2), as the target for cation substitution by metals such as Zn. Theoretical analysis of substitution of Ca^{2+} by Zn^{2+} has been carried out, and structural properties are expected to be extracted from x-ray absorption spectra.[4]

The present work analyzes the electronic structure of Fe-substituted HAP, using an embedded cluster density functional (ECDF) theoretical approach. Iron ions are among the trace ions which are present in bones and teeth. The concentration of iron in enamel was found to vary between 0 and 157 ppm, with a mean value 28 ppm.[5] The binding site, structural role, and function of Fe incorporated in bone are not well known. In the absence of atomic-scale experimental data we use atomistic simulations with simplified interatomic potentials to predict geometry of fourfold, fivefold, and sixfold oxygen coordination around Fe. The plausible geometries are then characterized by first-principles ECDF calcu-

lations. Mössbauer spectroscopy offers a site-specific probe of the iron environment, with results previously obtained from mineral apatatite, synthetic fluorapatite, bone, tooth, and synthetic carbonate apatite.[5–8] The ECDF predictions of site-dependent Mössbauer parameters can be combined with experiment to verify the local site properties.

This paper is organized as follows. Sample preparations and EPR and Mössbauer measurement procedures are presented in Sec. II. Section III contains a brief description of the theoretical methodology used. In Sec. IV we present calculated and experimental results with a detailed discussion; we summarize our conclusions in Sec. V.

II. EXPERIMENTAL PROCEDURES

Hydroxyapatite doped with 5 wt. % of natural iron (Fe-HAP) was prepared using a $Ca(NO_3)_2$ and $Fe(NO_3)_2$ solution (0.2 M) which was added dropwise to a $(NH_4)_2HPO_4$ aqueous solution (0.2 M) under constant stirring at 90 °C and pH=9±0.5.[9] After the addition the resulting precipitate was aged at 90 °C for 3 h. The precipitate was separated by filtration, repeatedly washed with boiling deionized water and dried at 100 °C for 24 h. Hydroxyapatite samples (0.2 g), with grain size in the range of $90 < d < 125$ μm, were analyzed by x-ray diffractometry ($a=b=9.4223$ Å, $c=6.8764$ Å), using a Seifert-FPM diffractometer operating with CuK_α radiation at 40 kV and 40 mA. The elemental concentrations of Ca, P, and Fe [(Ca+Fe)/P=1.59±0.04, Ca/P=1.51±0.04] were determined by inductively coupled plasma optical emission spectrometry using a Perkin Elmer ICP-OES Plasma 1000. In order to partially eliminate iron oxides linked to the hydroxyapatite surface, samples were treated with acid solution (H_2SO_4) of sodium dithionite, $Na_2S_2O_4$, during 2 h.

The ^{57}Fe Mössbauer spectrum was obtained by a commercial Mössbauer spectrometer (Wissel), operating in a constant-acceleration mode with a 25 mCi single line γ ray source of ^{57}Co:Rh . Detection of the 14.4 keV γ rays was achieved with a Kr proportional counter. The spectrum was collected at 4.2 K and 300 K; at 4.2 K, absorber and source were in a liquid helium bath cryostat. The absorption spectra

were computer fitted by the NORMOS program which uses the input parameters as a first approximation to fit the experimental curve. The EPR spectra of FeHAP samples were recorded at 300 K, with a Bruker ESP300E spectrometer, equipped with X band (9.5 GHz microwave frequency).

III. THEORETICAL CALCULATIONS: MODEL AND METHOD

A. Atomistic simulation approach

Atomistic simulations with parametrized interatomic potentials have become a powerful way to analyze material structures that contain up to many thousands of ions. In many ionic systems the interactions between ions are adequately described by pairwise potentials. In the present work we have used simple pair-wise Coulomb plus Buckingham-type potentials of the general form

$$V_{ij} = \frac{q_i q_j}{r_{ij}} + A e^{-r_{ij}/\rho} - \frac{C}{r_{ij}^6} \tag{1}$$

with parameters generated to best fit bulk lattice structure for the hydroxyapatite crystal. Hydroxyl radical groups are additionally modeled by a simple harmonic potential between O and H:

$$V_{\text{OH}} = 1/2 K (R - R_0)^2. \tag{2}$$

In order to accommodate the substituent iron ion and surrounding oxygen ion interactions we have added interatomic Lennard-Jones potentials of the form

$$V_{\text{LJ}} = \epsilon \left[\left(\frac{r_0}{r} \right)^{12} - 2 \left(\frac{r_0}{r} \right)^6 \right] \tag{3}$$

with parameters chosen to reproduce reasonable coordination number and ion radius sum rules.

A periodic cell scheme is used to represent the infinite ideal crystal. The potential parameters were obtained by fitting lattice structure of HAP using the program GULP, which optimizes the structure using the analytical conjugate gradient method.[10] The potential parameters obtained for ideal HAP were used as inputs for finite-volume nonperiodic simulations of the Fe-substituted structures. The relaxation calculations for Fe substitution at Ca(1) and Ca(2) sites have been performed using the generalized simulated annealing (GSA) scheme, which is a global stochastic optimization.[11] In a typical GSA simulation of a nonperiodic defect complex, an embedded cluster model is used, in which 131 ions are dynamical; i.e., free to move, and 5369 ions of the host HAP are fixed.

B. Embedded cluster density functional approach

We have used the discrete variational (DV) method in the calculation of the electronic structure for various clusters. The DV method is a first-principles molecular cluster approach based on local-density-functional (LDF) theory; details of this method are given in Refs.12,13. The matrix elements of Hamiltonian and overlap are evaluated by a numerical integration technique on a three-dimensional grid. In our calculations, the three-dimensional grid is divided into two regions: around the central Fe atom is placed a sphere of 2.4 a.u., where precise polynomial integrations are performed on a regular grid; outside the sphere the pseudorandom diophantine point generator is used. For the central Fe atom, $\sim 20\,000$ points are used inside the sphere and ~ 300 diophantine points outside; ~ 2000 diophantine points are employed for each Ca, P, O, H atom. In the present DV scheme, atomic basis functions ϕ are generated numerically as LDF solutions for free atoms or ions in a potential well. In order to solve the Poisson equation for the Coulomb potential efficiently, a model potential is created by least-squares fitting the true charge and spin density to a multicenter multipolar expansion within any desired level of precision. In the present work, we have limited the multipolar expansion to spherical functions about Ca, P, O, and H atoms, and some auxiliary expansion terms with $l = 0, 1, 2$ are considered about the central Fe atom to describe its surrounding highly distorted crystal field. Only the valence orbitals of the atoms except central Fe atom are kept in the variational space, while the inner core orbitals are frozen. Valence orbitals are chosen as $\{3d, 4s, 4p\}$ for Ca, $\{3s, 3p\}$ for P, $\{2s, 2p\}$ for O, and $\{1s\}$ for H. For central Fe atom, both its inner core and valence orbitals are included in variational space for the consideration of Sternheimer core polarization correction.[14] In order to simulate the external solid, the clusters are embedded in the charge densities of several layers of neighboring atoms. These embedding charge densities are obtained from atomic numerical LDF calculations, and are added to the cluster density in the construction of the Kohn-Sham Hamiltonian. The Vosko, Wilk, and Nusair (VWN) exchange-correlation formulation[15] was adopted in the potential.

A Mulliken-type atomic orbital population analysis is performed on the cluster eigenfunctions in order to determine effective atomic configurations and charges. The partial densities of states (PDOS) is constructed by broadening the cluster discrete energy levels by Lorentzians, with an appropriate half-width, and weighted by the Mulliken-type population of the atomic orbital.[13]

We have investigated the nature of the bonding structures at different sites by calculating the bond order (BO).[3,16] The BO, or Mulliken overlap population, between atoms p and q is defined as

$$\text{BO} = \sum_{i,\sigma} \sum_{k,m} n_{i\sigma} c_{ik\sigma}^* c_{im\sigma} S_{km}, \tag{4}$$

where S_{km} is the overlap integral between basis functions χ_k and χ_m centered at atoms p and q, respectively, and σ is the spin index.

Density functional methods have been applied with success to the theoretical predictions of Mössbauer hyperfine parameters. The isomer shift is defined as[14]

$$\text{IS} = 2/3 e^2 \pi Z S(Z) \Delta \langle r^2 \rangle [\rho_A(0) - \rho_S(0)] \equiv \alpha \Delta \rho(0), \tag{5}$$

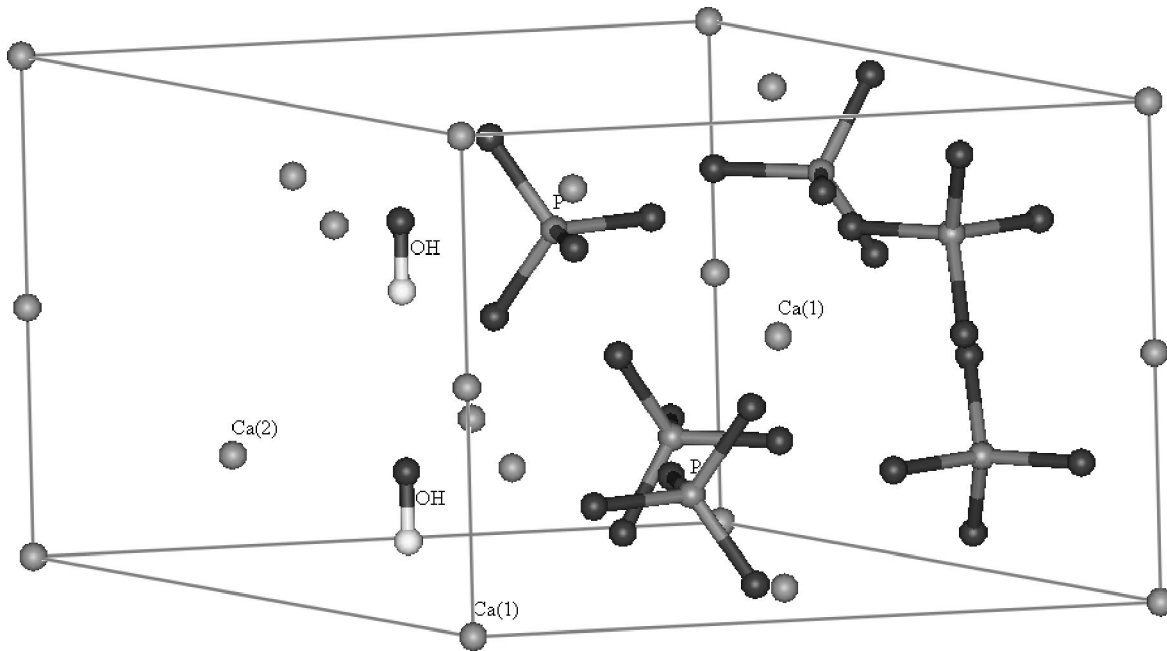where the term in square brackets is the difference between the electronic density at the nucleus in the absorber A

FIG. 1. Hydroxyapatite Ca$_{10}$(PO$_4$)$_6$(OH)$_2$ unit cell. Ca(1) and Ca(2) indicate two different calcium sites in HAP (see also Fig. 2).

and source S. In practice, the isomer shift relative to iron metal is[17]

$$IS = -0.228\rho(0) + 33.638 \ \ (mm/s), \tag{6}$$

where $\rho(0)$ includes $3s$ and $4s$ contributions at the nucleus.

The quadrupole splitting for ^{57}Fe is given by[14,17]

$$QS = 1/2e^2V_{zz}Q\left(1 + \frac{\eta^2}{3}\right)^{1/2}$$

$$= 10.109V_{zz}Q\left(1 + \frac{\eta^2}{3}\right)^{1/2} \ \ (mm/s), \tag{7}$$

where Q is the quadrupole moment of the nucleus with spin $I = 3/2$ in the excited state of the 14.4 KeV Mössbauer transition [$Q = 0.16$ b (Ref. 18)], V_{zz} is the electric field gradient (in atomic units) and η the asymmetry parameter

$$V_{ij} = -\int \rho(\vec{r})(3x_ix_j - \delta_{ij}r^2)/r^5 dv$$

$$+ \sum_q Z_q(3x_{qi}x_{qj} - \delta_{ij}r_q^2)/r_q^5(x_i, x_j = x, y, z), \tag{8}$$

$$\eta = \frac{V_{xx} - V_{yy}}{V_{zz}}, |V_{zz}| > |V_{yy}| > |V_{xx}|. \tag{9}$$

The first term is the electronic contribution, calculated in the DV method as the integral over the cluster valence electronic density, and the second term is the point-charge contribution (nucleus and frozen core) of atoms surrounding the central Fe atom. The Fe core electrons are included in the self-consistent field (SCF) calculations, so the Sternheimer core polarization correction factor[14] is not considered here. The Fermi or contact contribution to the magnetic hyperfine field H_c is given by

$$H_c = -(8\pi/3)g_e\mu_B\frac{1}{2}[\rho\uparrow(0) - \rho\downarrow(0)], \tag{10}$$

where μ_B is the Bohr magneton and the term in brackets is the difference between the electron density at the Fe nucleus for spin up and spin down. The spin dipolar field H_D is defined as

$$H_D = -g_e\mu_B M_{zz}, M_{zz}$$

$$= \frac{1}{2}\int [\rho\uparrow(\vec{r}) - \rho\downarrow(\vec{r})](3z^2 - r^2)/r^5 dv, \tag{11}$$

where M_{zz} is the largest component of the H_D tensor. The axis of quantization of electron spin **S** is assumed to be parallel to the principal EFG axis for the sake of convenience. The total measured magnetic hyperfine field H_F at the Fe nucleus is written as $H_F = H_c + H_D$.

IV. RESULTS AND DISCUSSION

A. Atomistic simulations

1. Pure hydroxyapatite structure and force field model

Hydroxyapatite has hexagonal structure with symmetry space group $P6_3/m$ and lattice parameters $a = b = 9.432$ Å, $c = 6.881$ Å.[19] There is one formula unit Ca$_{10}$(PO$_4$)$_6$(OH)$_2$ (44 atoms) per unit cell. The phosphate tetrahedra PO$_4$ are linked by cations Ca, which are arranged on two nonequivalent sites. Ca^{2+} at the special site $4f$, denoted Ca(1), is sixfold coordinated to 3O(1) and 3O(2) atoms while Ca^{2+} at the site $6h$, denoted Ca(2), is sixfold coordinated to 4O(3), O(2) and O$_H$ atoms (see Figs. 1 and 2). Some authors have preferred to describe Ca(1) as nine-fold coordinated [additional O(3) found at 2.81 Å] and Ca(2) as sevenfold coordinated [additional O(1) at 2.70 Å].[20–22] Considering

(A)
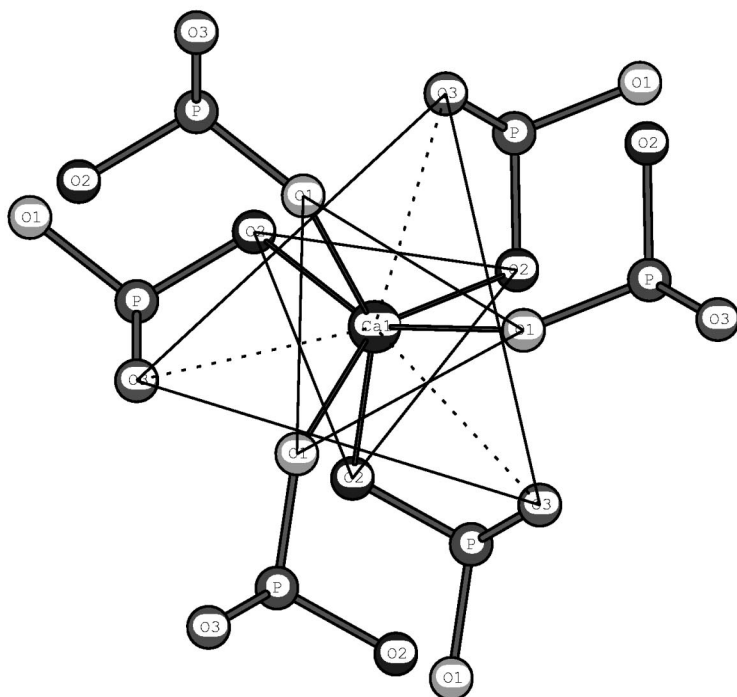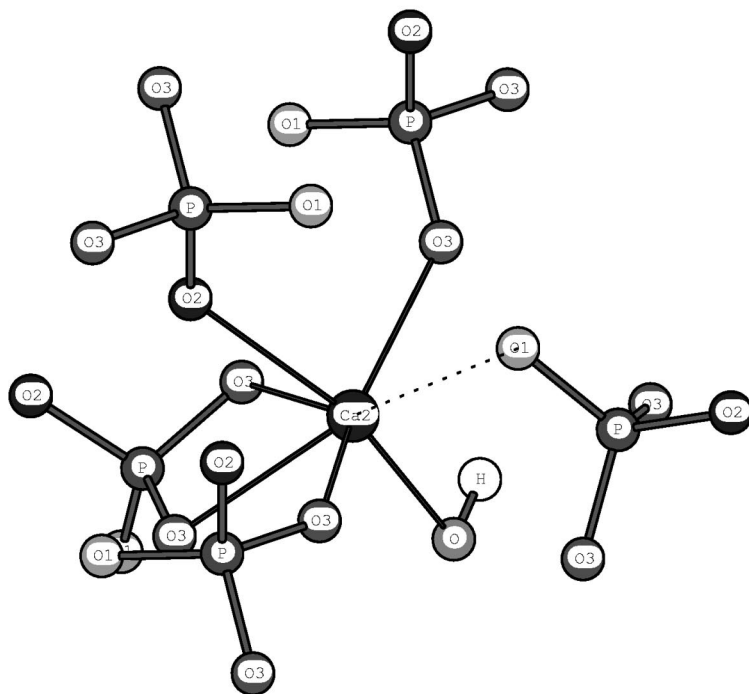
FIG. 2. Local geometries of the two different Ca sites in pure hydroxyapatite. (a) Ca(1) site with C_3 symmetry; (b) Ca(2) site.

(B)

the different sites at which the Ca and O atoms are found, the chemical formula can be rewritten as $Ca(1)_4Ca(2)_6[PO(1)O(2)O(3)_2]_6(O_HH)_2$. Recent studies of cation substitution in fluorapatites (FAP's) are of special relevence to our own interest in substituted HAP.[21,22] In those studies semiempirical interatomic potentials were used to predict cation (Cs and lanthanide) diffusion within the bulk material.

TABLE I. Empirical force field parameters for hydroxyapatite. A, ρ, and C are Buckingham coefficients; K, R_0 describe the O-H harmonic bond interaction, see Eqs. (1) and (2). The cutoff radius is 12 Å for the Buckingham potentials.

Ion/pair	A(eV)	ρ(Å)	C(eV Å^6)	Charge
Ca(1)				$+0.88$
-O(1)	16008.5	0.245	240.6	
-O(2)		0.244		
-O(3)		0.246		
Ca(2)				$+0.88$
-O(1)	16008.5	0.254	240.6	
-O(2)		0.243		
-O(3)		0.247		
-O_H		0.240		
P				$+3.40$
-O(1)	9034.208	0.198	19.9	
-O(2)		0.197		
-O(3)		0.196		
O(1)				-1.20
-O(1)	1388.773	0.362	175.0	
-O(2)		0.374		
-O(3)		0.366		
O(2)				-1.20
-O(2)	1388.773	0.348	175.0	
-O(3)		0.362		
O(3)				-1.20
-O(3)	1388.773			
	K(eV Å^{-2})	R_0 (Å)		
O_H				-0.58
H				$+0.38$
O_H-H	32.6	0.95		

In the present work we have modeled the hydroxyapatite structure using pairwise Coulomb plus Buckingham-type potentials and harmonic potentials as described in Sec. III A. The corresponding potential parameters $\{A, \rho, C, K, R_0, q\}$ have been fitted to the experimental HAP lattice structure using the program GULP, and are summarized in Table I. Note that the phosphorus and oxygen parameters were initially taken from a previous fit to $AlPO_4$ (Refs. 23,24) and refined in the present calculations for HAP to allow for nonequivalent oxygen ions. The O-O Buckingham interactions modify the Coulomb repulsion and ensure the tetrahedral arrangement of oxygen atoms around the phosphorus atom.[23]

The energy-minimized structures of HAP obtained using our potential parameters are compared with experimental values in Table II, together with the elastic constants for the isostructural natural mineral apatite containing OH, F, and Cl.[25] As can be seen in Table II, the structure of HAP was reproduced very well, including lattice constants, Ca-O distances and bond angles within the phosphate group. However, the calculated elastic constants only semiquantitatively resemble the natural apatite data. Experimental HAP elastic constants would be desirable for improving the elastic constants fit.

2. Fe^{2+}, Fe^{3+} substitution at calcium sites

Due to their $3d$ electron configuration, Fe^{2+} and Fe^{3+} cations have flexible coordination geometries fourfold, fivefold, and sixfold in their compounds. For trivalent Fe^{3+} substitution at a Ca^{2+} site, we investigated the defected and nonstoichiometric case to consider charge compensation. At the Ca(1) site, a nonstoichiometric system $Ca_{10-x}(PO_4)_{6-x}(HPO_4)_x(OH)_2$, $x=1$ was introduced, while another system $Ca_{10-x}(PO_4)_6(OH)_{2-x}$, $x=1$ characterized by vacancies at hydroxyl and Ca(2) sites was considered for the Fe^{3+} substitution at Ca(2) sites.

TABLE II. Comparison of experimental and calculated lattice structure and elastic properties for hydroxyapatite. Note that the experimental elastic constants are for natural apatite containing OH, F, and Cl.

$Ca_{10}(PO_4)_6(OH)_2$	experimental	calculated	difference	%
Volume (Å^3)	530.139	528.137	-2.00	-0.38
a (Å)	9.432	9.379	-0.053	-0.56
c (Å)	6.881	6.937	0.056	0.81
Ca(1)-O(1) (Å)	2.408	2.405	-0.003	-0.12
Ca(1)-O(2)	2.454	2.438	-0.016	-0.65
Ca(1)-O(3)	2.810	2.791	-0.019	-0.68
Ca(2)-O(1)	2.702	2.693	-0.009	-0.33
Ca(2)-O(2)	2.356	2.357	0.001	0.04
Ca(2)-O(3)	2.36, 2.516	2.378, 2.508	0.018, -0.008	0.76, -0.32
Ca(2)-O_H	2.388	2.387	-0.001	-0.04
O(1)-P-O(2) (deg.)	110.7	110.5	-0.2	-0.18
O(3)-P-O(2)	107.7	108.0	0.3	0.28
O(3)-P-O(1)	111.5	111.1	-0.4	-0.36
C_{11} (10^{11}dyn/cm^2)	16.67	14.37		
C_{13}	6.55	7.598		
C_{33}	13.96	26.84		
C_{55}	6.63	5.19		

TABLE III. Lennard-Jones potential parameters for Fe-O interaction in different coordination environments at Ca sites in HAP.

Ion	Site	Coordination	ϵ(eV)	r_0(Å)
Fe^{2+}	Ca(1)	6	1.3	2.16
		5	0.8	2.01
		4	0.4	2.01
	Ca(2)	6	1.2	2.16
		5	0.6	2.01
		4	0.5	2.01
Fe^{3+}	Ca(1)	6	1.5	2.03
		5	1.6	1.87
		4	1.2	1.87
	Ca(2)	6	1.6	2.03
		5	1.4	1.87
		4	1.2	1.87

The Lennard-Jones potential parameters listed in Table III result from a detailed mapping of the the response of Fe to different coordination environments. These parameters were chosen to reproduce observed Fe-O bond lengths with reasonable bond energies for fourfold, fivefold, and sixfold coordination. The relaxed structures of Fe^{2+} and Fe^{3+} substitution at Ca(1) and Ca(2) sites were obtained by performing GSA simulations, with results listed in Tables IV and V. As seen from the tables, the first neighbor Fe-O distances range from 1.94–2.27 Å for Fe^{2+} to 1.80–2.14 Å for Fe^{3+}, which is considerably shorter than those of Ca-O, 2.36 Å$<R$ <2.51 Å. The fourfold, fivefold, and sixfold coordination geometries are tetrahedral, pyramidal and distorted octahedral, respectively.

For Fe^{2+} substitution, the stoichiometry of HAP is always maintained; the "missing" oxygen in fourfold and fivefold coordination are merely displaced to considerable distance by lattice relaxation driven mostly by ionic radii. In order to discuss the relative stability of different coordination and the two Ca sites, we calculated the potential energy of the relaxed systems shown in Tables IV and V. Since the empirical Fe-O Lennard-Jones interaction energy parameters ϵ are dif-

ferent in varying coordinations and Ca sites, a simple procedure was performed to "renormalize" the local Fe-O Lennard-Jones interactions. The system potential energy can be written as $W_{total} = W_{Fe-O} + W'$, where the Fe-O interaction W_{Fe-O} depends linearly on ϵ. Scaling W_{Fe-O} to the common value $\epsilon = 1.0$ eV permits comparison of binding energy differences in different coordination at different sites. The main results are as follows.

(1) For Fe^{2+} substitution, we find the binding energy order $E(4)<E(5)<E(6)$ at the Ca(1) site and also $E(4)<E(5)<E(6)$ at the Ca(2) site. The most favored geometry is the sixfold Ca(2) site (see Fig. 3) which is followed by sixfold Ca(1) and fivefold Ca(2) sites.

(2) For nonstoichiometric Fe^{3+} substitution, the corresponding energy ordering is $E(5)<E(6)<E(4)$ at the Ca(1) site and $E(6)<E(4)<E(5)$ at the Ca(2) site. So, the Fe^{3+} low coordination geometry is more stable due to the defects. Here the most stable geometry is the fourfold Ca(1) site, followed by fivefold Ca(2). Figure 4 displays the geometric structure of the fourfold Ca(1) site.

B. Experimental Mössbauer and EPR spectra of FeHAP

There have appeared several x-ray structural and Mössbauer (MB) studies of iron-containing apatites, either occurring naturally,[26] produced by high-temperature diffusion of ^{57}Fe into a natural apatite,[7] or by solid phase reaction.[8] By comparing these reports we may verify the variability of Fe^{2+} site preference, depending upon conditions of preparation, availability of oxygen, and hydroxyl content. Ok prepared ^{57}Fe-doped specimens by diffusing iron into natural apatite samples (a mixture of F, Cl, and OH occurring on the *c*-axis channels), using both powder and single crystal starting material. The diffusion was carried out at ~1000 °C for several days under nitrogen atmosphere. A color change from light yellow to white was observed, and considering the FeF_2 (or FeI_2) source, we may suppose that OH was largely removed from the samples, resulting mostly in surface-enriched iron-doped fluorapatite. Noting that the ideal (unrelaxed) Ca(1) site has C_3 symmetry, with corresponding greatly simplified crystal field levels, and a zero value of the

TABLE IV. Mean interatomic distances, distribution widths, and relative binding energies obtained for Fe^{2+} at Ca sites with different coordinations in HAP. The zero of the energy scale is set at the binding energy of pure HAP.

Ion	Site	Coordination	Mean R (deviation)(Å)	Min R (Å)	Max R (Å)	Relative binding energy E (eV)
Fe^{2+}	Ca(1)	6 pure Ca	2.43(0.022)	2.41	2.45	0.00
		6 unrelaxed				2.16
		6 relaxed	2.22(0.026)	2.19	2.27	4.08
		5	2.04(0.043)	1.97	2.08	3.43
		4	1.99(0.039)	1.94	2.04	3.19
Fe^{2+}	Ca(2)	6 pure Ca	2.41(0.073)	2.35	2.51	0.00
		6 unrelaxed				2.47
		6 relaxed	2.21(0.032)	2.16	2.25	4.51
		5	2.02(0.031)	1.99	2.06	3.85
		4	2.04(0.076)	1.96	2.16	3.24

TABLE V. Mean interatomic distances, distribution widths, and relative binding energies obtained for Fe^{3+} at Ca sites with different coordinations in HAP. The zero of the energy scale is set at the binding energy of pure HAP.

Ion	Site	Coordination	Mean R (deviation) (Å)	Min R (Å)	Max R (Å)	Relative binding energy E (eV)
Fe^{3+}	Ca(1)	6 pure Ca	2.43(0.022)	2.41	2.45	0.00
		6 unrelaxed				-2.87
		6 relaxed	2.04(0.021)	2.02	2.09	2.74
		5	1.89(0.026)	1.86	1.93	1.82
		4	1.85(0.022)	1.82	1.88	3.21
Fe^{3+}	Ca(2)	6 pure Ca	2.42(0.078)	2.35	2.51	0.00
		5 unrelaxed				-6.35
		6 relaxed	2.08(0.046)	2.00	2.14	0.03
		5	1.87(0.016)	1.85	1.89	1.04
		4	1.84(0.024)	1.80	1.87	0.11

asymmetry parameter, Ok constructed a molecular orbital model for the two sites, and gave a consistent interpretation of the two-site MB spectra. He found an approximately random occupancy of the four Ca(1) and six Ca(2) sites, with nearly identical IS of 1.09 and 1.10 mm/sec, characteristic of Fe^{2+}. At a temperature of 4.2 K the observed QS were ~3.7 and ~2.2 mm/sec, respectively. The two lines behave differently with increasing T; the large value falling to 3.47 mm/sec at 300 K, and the smaller value falling more rapidly to 0.98 mm/sec. In Ok's MO model, with various simplifying assumptions, the crystal field splitting of Fe $3d$ levels at the trigonal Ca(1) site is 12 times as large as the spin orbit splitting, leading to very little mixing of the ground state ($M=\pm2$) orbital, consistent with the observed weak tem-

perature dependence. On the other hand, the lower symmetry of the Ca(2) site is supposed to completely lift the orbital M_L degeneracy, giving a "gap" between ground and first excited states of 3.6 times the spin-orbit splitting, again consistent with the observed rapid decrease of QS of the second spectrum with increasing temperature. By adjustment of neighboring ion charges to best fit the T dependence, a MO ground state was proposed for the Ca(2) site.

Khudolozhkin et al.[8] prepared fluorapatite by solid-phase synthesis according to the reaction Ca$_2$P$_2$O$_7$+(3$-y$)CaO +yFeO+CaF$_2$=> (Ca$_{10-y}$Fe$_y$)(PO$_4$)$_6$F$_2$ with y=0.01, 0.025, 0.10, 0.15, and 0.20. The miscibility limit at 1200 °C was found at the composition (Fe$_{1.5}$Ca$_{8.5}$)(PO$_4$)$_6$F$_2$ by x-ray measurement of the lattice parameters. Following the assign-
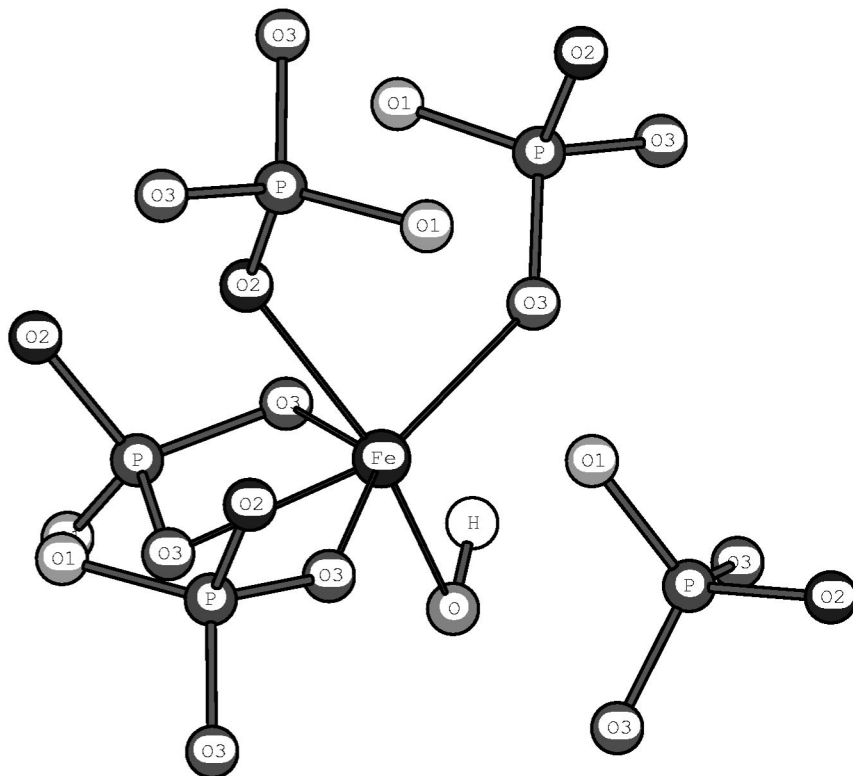

FIG. 3. Geometry of the most stable cluster found from simulations on Fe^{2+}-HAP: sixfold coordination at the Ca(2) site.
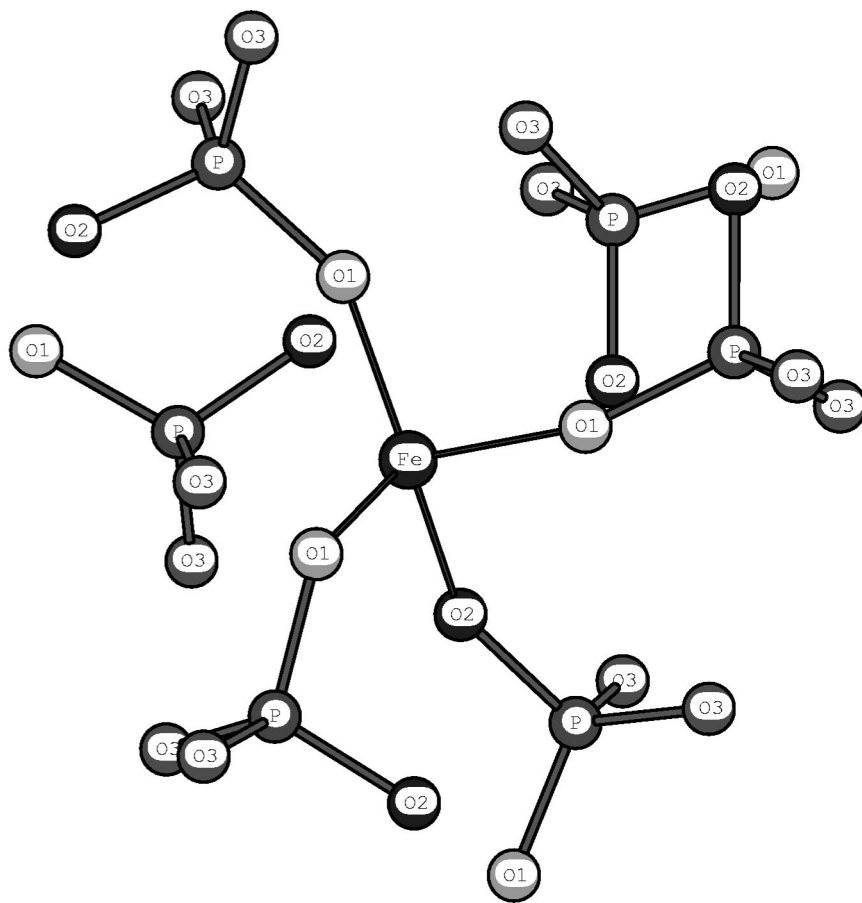
FIG. 4. Geometry of the most stable cluster found from simulations on Fe^{3+}-HAP: fourfold coordination at the Ca(1) site.

ment of Ok, they measured the 300 K Mössbauer spectra for IS of Ca(1) and Ca(2) as 1.30 and 1.45 mm/sec, respectively. The corresponding QS were found as 2.40 and 1.00 mm/sec. Taking the ratio of Ca(1) to Ca(2) line intensities, they found that the Ca(1) site is strongly preferred at higher Fe concentrations, but is statistical at low concentration. The authors note that the larger chemical shift at the Ca(2) site indicates a greater effective Fe^{2+} ionicity there.

In comparing the results of Ok and Khudolozhkin *et al.*,[8] we see some notable differences between site occupancy IS and QS which may be attributed to the different methods of sample preparation. We also note that the Ca(1), Ca(2) site identification in the two works is dependent upon assumptions of a preserved C_3 symmetry at Ca(1) and a simplified empirical crystal field model. Hence, the more recent work of Hughes *et al.*[26] on iron-bearing natural apatite is quite revealing, confirming earlier reports[27] from optical spectroscopy that small amounts of Fe drive a lattice transformation to the monoclinic $P2_1/m$ structure, associated with small deformations of the $P6_3/m$ Ca(2) site. By careful refinement of x-ray diffraction data on a natural apatite crystal containing >1.2 wt. % iron, Hughes *et al.* concluded that the degenerate $P6_3/m$ Ca(2) site splits into six nonequivalent sites Ca(2a,b,c), Ca(2a,b,c)′ and that these sites are preferentially occupied by iron, with essentially equal occupancy. In contrast, the Ca(1) sites are found to be essentially not occupied by Fe, contrary to the model used by Ok and Khudolozhkin. Hughes *et al.* justify their assignment on the grounds of

a known large crystal field stabilization energy of the $Fe^{2+}d^6$ configuration, contrasting to the site preference of high spin $Mn^{2+}d^5$, and find supporting cases in the mineral literature. Thus, there are good experimental grounds for doubting the original site assignments. Now with respect to the present work, we note that preparation procedures (precipitation synthesis) and the resulting products (hydrated, nanocrystalline, and polycrystalline, pure OH channel anion with no halide content) are chemically different, and quite possibly structurally different from the materials previously studied. We present elsewhere a detailed analysis of Mössbauer and EPR studies of FeHAP prepared with 1, 5, and 10 wt.% iron under various conditions, and subjected to heat treatment, and cycles of oxidation and reduction. Our experimental results show that the number of sites and their relative occupancy varies with Fe concentration and conditions of preparation. The 5 wt.% concentration samples are resolved into five sites, which can be associated with a surface species, two Fe^{2+}, and two Fe^{3+}, presumably distributed over both Ca(1) and Ca(2) sites. Analysis of line intensities suggests that the sites are approximately equally occupied; the surface contribution can be decreased by dithionite washing. Under suitable preparation conditions, the surface oxide particle size can be reduced to a range (<10 nm) where magnetic ordering is no longer observed. Figure 5 shows the Mössbauer spectrum of a typical as-synthesized hydroxyapatite sample doped with 5 wt.% of natural Fe; parameters of the five component lines are given in Table VI. At 4.2 K a spectrum
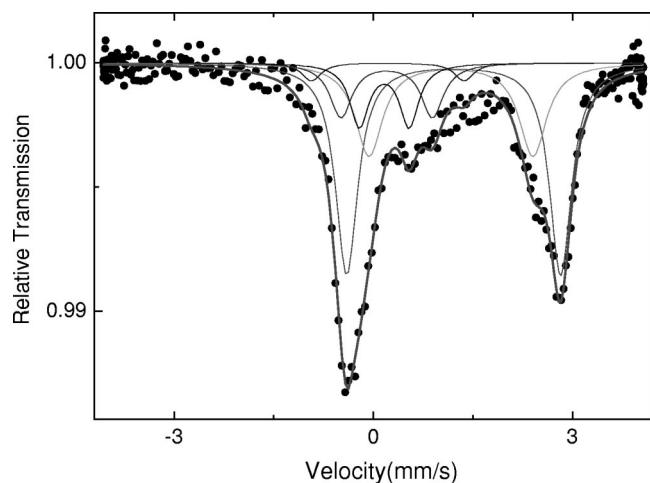
FIG. 5. Mössbauer spectrum of the as-synthesized 5 wt. % Fe-HAP measured at 4.2 K.

was measured at high velocity in order to observe any magnetic splitting due to iron oxides not contained within the hydroxyapatite structure such as was seen in 1 wt.% samples; however, the spectrum showed only paramagnetic components. The model proposed here to analyze the spectra has five doublets, where two Fe species ($D1$, $D2$) have hyperfine parameters typical of Fe^{2+}, and the other three species ($D3$, $D4$, $D5$) correspond to Fe^{3+}. The last species ($D5$) shown in Table VI has an IS and QS similar to that of very small particles of hematite (α-Fe$_2$O$_3$) in the superparamagnetic regime.[28] It may appear at first that fitting five lines to the spectrum of Fig. 5 is either unreliable or unverifiable; however, these parameters were not obtained in isolation, but in parallel with a series of measurements and fits to distinct specimens with different Fe concentrations and different treatment regimes. In particular, the Fe^{3+} species can be clearly identified and isolated in oxidized samples, and the IS, QS parameters can be transferred to as-prepared and reduced samples. The QS of both Fe^{2+} and Fe^{3+} spectra de-

TABLE VI. Mössbauer hyperfine parameters of as-prepared 5 wt % FeHAP sample measured at 4.2 and 300 K. The values in parentheses are estimated uncertainties, an F indicates a value fixed by reference to fits on an extensive set of specimens.

Assignment	Temp. (K)	IS[a] (mm/s)	QS (mm/s)	Width (mm/s)	Area (%)	Comments
$D1$	4.2	1.21(3)	3.22(7)	0.40(F)	47	Fe^{2+}
	300	1.20(5)	2.43(3)	0.43(F)	31	
$D2$	4.2	1.17(6)	2.40(8)	0.50(F)	25	Fe^{2+}
	300	1.14(7)	1.80(7)	0.50(F)	27	
$D3$	4.2	0.21(F)	2.25(F)	0.35(F)	4	Fe^{3+}
	300	0.23(F)	1.72(F)	0.35(F)	6	
$D4$	4.2	0.22(F)	1.38(F)	0.34(F)	12	Fe^{3+}
	300	0.22(F)	1.14(F)	0.40(F)	18	
$D5$	4.2	0.20(F)	0.75(F)	0.40(F)	12	Surface Fe^{3+}
	300	0.22(F)	0.69(F)	0.40(F)	18	

[a]The measured isomer shift(IS) are relative to α-Fe.

crease notably with temperature, being reduced by ~25% and 17–24%, respectively, from 4.2 to 300 K. Some variations in spectra are seen, depending upon method of preparation (starting from Fe^{2+} or Fe^{3+} in solution, treatment to remove surface species, cycles of oxidation, and reduction, etc.), which will be discussed in detail elsewhere. However, the general features aid in an interpretation of the 1, 5, and 10 wt. % data, and we suggest the following.

(i) Site occupancy for Fe in the apatite structure is sensitive to the conditions of preparation, and the anion (OH, Cl, F) content. Surface diffusion under anhydrous conditions, or anhydrous high temperature synthesis may well produce quite different site distributions.

(ii) Once deposited in the HAP lattice, Fe^{2+} may be subject to subsequent oxidation. This is observed via the change in Mössbauer intensities with time in the precipitation produced 5 and 10 wt. % samples. It is thus possible that Fe^{2+} is deposited initially in both sites, and that oxidation occurs preferentially at one site, a process which is independent of the initial energy ranking of the Ca(1) versus Ca(2) sites.

(iii) Despite the variability in spectra due to sample preparation and treatment discussed above, we may extract some "typical" IS and QS parameters, and comment on relative site occupancies as follows.

(1) The surface Fe^{3+} species, $D5$ with IS, QS of 0.20, 0.75 mm/s at 4.2 K changes very little with temperature, and is similar to that of hematite, consisting of superparamagnetic nanoparticles.

(2) Of the two Fe^{2+} bulk sites, $D1$ with IS, QS of 1.21, 3.22 mm/s at 4.2 K which we assign to Ca(1) (see the following theoretical analysis) is preferentially occupied (~2:1). The QS falls to 2.43 mm/s at 300 K.

(3) The second Fe^{2+} site $D2$, which we assign to Ca(2), has IS, QS of 1.17, 2.40 mm/s at 4.2 K, and QS falls to 1.80 mm/s at 300 K.

(4) Of the two Fe^{3+} bulk sites, $D4$ with IS, QS of 0.22, 1.38 mm/s at 4.2 K which we assign to fourfold coordination either at Ca(1) or Ca(2), is preferentially occupied (~3:1). The QS falls to 1.14 mm/s at 300 K.

(5) The remaining Fe^{3+} site, $D3$ with IS, QS of 0.21, 2.25 mm/s at 4.2 K is assigned to sixfold coordinated Ca(2). The QS falls to 1.72 mm/s at 300 K.

As can be seen from these data, the MB spectra of Fe-doped precipitation preparations of HAP are considerably different from those of mineral apatites and dry synthesis fluorapatite, as well as tooth and bone, as summarized in Table VII. As mentioned above, they also show variability as a function of synthesis conditions and processing; once understood, this variability can be used to advantage for a detailed characterization of this complex and interesting material. In the following theoretical sections we achieve a partial understanding of the local lattice environment through atomistic simulations and electronic structure calculations. However, a complete match between theory and experiment is not to be expected.

The EPR spectrum of FeHAP, shown in Fig. 6, is composed of a signal at $g = 4.23$ and a broad line at $g \approx 2.13$ (~0.089 T peak to peak linewidth). The physical interpretation of the $g = 4.23$ Fe^{3+} resonance has been well studied by

TABLE VII. Previously reported experimental Mössbauer isomer shift (IS), quadrupole splitting (QS), and absolute value of hyperfine magnetic field (H_F) of Fe-doped apatite.

Sample	Temperature (K)	IS (mm/s)	QS (mm/s)	H_F (KOe)
Fe-doped natural apatite[a]	300	1.09	3.47	
		1.10	0.98	
	4.2		~3.70	
			~2.20	
Fe-doped fluorapatite[b]	300	1.30(4)	2.40(1)	
		1.45(7)	1.00(4)	
Enamel soaked in Fe^{2+} solution[c]	85	1.40	3.44	
Teeth (*in vivo*)[c]		1.27	2.86	
Fe^{3+} in carbonate apatite[d]	85	0.35–0.48	0.76–0.85	488–500
Enamel soaked in Fe^{3+} solution[d]		0.46	0.72	
Bone (*in vivo*)[d]		0.46	0.76	516
Teeth (*in vivo*)[d]		0.48	0.78	505

[a]From Ref. 7.
[b]From Ref. 8.
[c]From Ref. 5.
[d]From Ref. 6.

several authors[29–31] using different glasses doped with iron ions. According to these studies, for strong crystal field environment with Hamiltonian

$$H = \beta g_0 \mathbf{H_0} \cdot \mathbf{S} + D[S_z^2 - 1/3S(S+1)] + E(S_x^2 - S_y^2) \quad (12)$$

and $E \gg g_0 \beta H_0$ and $D=0$, the $S=5/2$ sixfold degeneracy is split into three Kramers doublets with $W=0$ and $\pm 2(7E)^{1/2}$. Using a perturbation theory treatment, Castner *et al.* showed[29] that the $W=0$ doublet has a $g=30/7=4.3$. Similarly, in FeHAP the Fe^{3+} $g=4.23$ isotropic species can be attributed to isolated high spin, $S=5/2$, Fe^{3+} ions in distorted octahedral and/or tetrahedral bulk sites. The broad line at $g=2.10$ is frequently observed in the ESR spectra of superparamagnetic and ferromagnetic iron particles, and was well studied in iron precipitates in glasses.[31] The behavior of this resonance (intensity and linewidth) with the decrease of

FIG. 6. Room-temperature EPR spectrum of the as-synthesized 5 wt. % FeHAP.

sample temperature and with the HAP surface chemical treatment will be discussed in detail in a subsequent work, for hydroxyapatite samples with iron content of 1, 5, and 10 wt. %. The broad line can be associated with interaction of exchange-coupled iron pairs as is seen in small iron oxide particles; as discussed below, these are probably nanoparticles of hematite. The EPR spectra of samples chemically treated with sodium dithionite did not show this broad line, indicating that Fe^{3+} oxides, attached to the HAP surface, are produced during the HAP precipitation. The above results are not completely in accord with those of Bauminger *et al.*[5] and Mayer *et al.*[6] who proposed that Fe^{3+} is not incorporated in the apatite lattice but instead remains attached to the HAP lattice in the form of FeOOH particles.

C. Density functional calculations: electronic structure

Using both unrelaxed geometries and the relaxed ones described above, we carried out ECDF calculations on clusters centered at Fe, with 44 atoms in the active variational space while ~5400 ions of the host HAP are included to simulate the crystal potential. The results of Mulliken charge analysis are summarized in Table VIII. For the Fe^{2+}-HAP case, the total charges of iron ions located either at Ca(1) or Ca(2) sites with sixfold, fivefold, and fourfold coordination are very close to the formal value of +2. The neighboring oxygen atoms are far from their ideal −2 valent states. The calculated bond orders of Fe-O bonds are close to zero, indicating an ionic nature. In contrast, the bond orders of P-O bonds in the tetrahedral PO_4 group range from 0.54 to $0.73e$ consistent with their mostly covalent character. For the Fe^{3+}-defected HAP case, the resultant charges on the iron atom are $\sim 0.5e$–$0.7e$ less than the formal value +3 due to considerable covalent mixing with neighbors.

It would be very desirable to obtain confirming experimental data on the predominant site geometry and valence
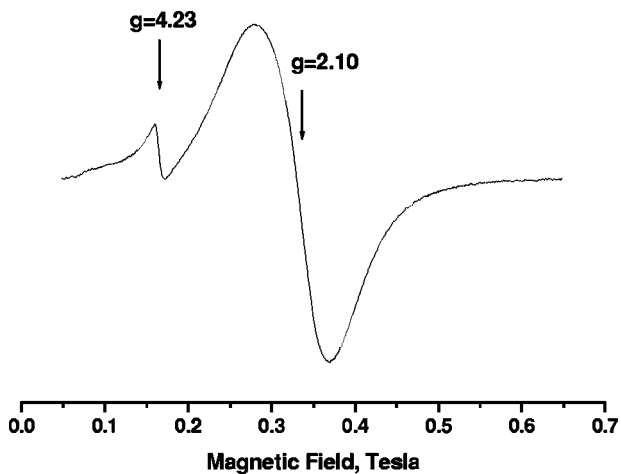
TABLE VIII. Mulliken charges for iron and nearest neighboring oxygen atoms in HAP calculated at Ca(1) and Ca(2) sites with different coordinations.

Site		Fe^{2+}:HAP	Fe^{3+}:HAP with defect
Ca(1)	Coordination	Fe^{2+}, O	Fe^{3+}, O
	sixfold	$+1.89, -1.52$	$+2.48, -1.53$
	fivefold	$+1.90, -1.51$	$+2.48, -1.49$
	fourfold	$+1.86, -1.51$	$+2.47, -1.45$
Ca(2)		Fe^{2+}, O, O$_H$	Fe^{3+}, O
	sixfold	$+1.81, -1.49, -1.63$	$+2.32, -1.48$
	fivefold	$+1.77, -1.47, -1.63$	$+2.31, -1.51$
	fourfold	$+1.74, -1.49$	$+2.26, -1.46$

state of the impurity. Mössbauer spectra reported here for iron substituted HAP, do provide useful data on the Fe valence and local environment. Our calculated Mössbauer parameters: isomer shift, quadrupole splitting, and magnetic hyperfine field for all Fe^{2+} and Fe^{3+} substituted HAP geometries are shown in Tables IX and X. The absence of detectable magnetic features in the experimental MB spectra is presumably due to rapid fluctuation of the moment direction. The isomer shifts listed in Table IX are typical of sixfold, fivefold, and fourfold Fe^{2+} ions,[32] and consistent with our Mulliken charge and bond order analysis. Furthermore, the most favored predicted geometry of Fe^{2+} substitution, sixfold at the Ca(2) site gives QS of -2.23 mm/s while the second-ranked sixfold Ca(1) site gives 4.42 mm/s. Considering the experimental QS values for $D1$ and $D2$ of $|QS|=3.22$ and 2.40 mm/s respectively, we assign $D1$ to the sixfold relaxed Ca(1), and $D2$ to the relaxed sixfold Ca(2)sites. The greater spectral linearea of $D1$ compared to $D2$ suggests a

greater occupancy of the Ca(1) site, contrary to the (slight) predicted energy preference for Ca(2). In both Ca(1) and Ca(2) sites, we predict a too-rapid decrease of QS with T, indicating that the calculated first crystal-field excitation energy is too small. Site assignment for the Fe^{3+} species is also nontrivial. For example, Mayer *et al.* proposed that Fe^{3+} ions are present in the FeOOH form both in biological and synthetic apatites. However, recent experiments show that pure α-FeOOH has IS of 0.34 mm/s and QS of 0.28 mm/s.[33] Apparently, the FeOOH QS is very different from our experimental values and the result Mayer *et al.* obtained in Fe^{3+} substituted HAP. According to our simulations, Fe^{3+} fourfold Ca(1) geometry is the most stable among the six Fe^{3+} substituted structures studied, by a relatively large factor. The apparently dominant species $D4$ (area $D4:D3=3:1$) has a QS of 1.38 mm/s, significantly greater than the calculated value of 0.84 mm/s at Ca(1). The calculated QS of 1.46 mm/s at the fourfold Ca(2) site is quite consistent with experiment, despite the predicted energy disadvantage. The minority species $D3$, with QS of 2.25 mm/s is more readily identifiable with sixfold relaxed Ca(2) with predicted QS of 1.64 mm/s. In the following paragraphs we explore further the great sensitivity of calculated QS to local geometry, static and dynamic temperature effects on energy levels and their occupancy, and upon computational details. At this point, we can assert simply that relative magnitudes of calculated first-principles QS appear to give a sensible assignment of sites and coordination, while atomistic energies seem to be a useful, but less reliable indicator. Bearing in mind the coexistence of fourfold and sixfold Fe^{3+} species in "simpler" materials such as Fe$_3$O$_4$ magnetite, we need not be surprised by the assignments given here.

In order to further explore the nature of the chemical bonding and chemical environment in Fe^{2+}/Fe^{3+} subsitu-

TABLE IX. Calculated Mössbauer isomer shift, quadrupole splitting QS(T), and hyperfine magnetic field $H_F = H_c + H_D$ (see text) of Fe^{2+}-HAP. Temperatures of 0 and 300 K are presented.

Ion/site	Coordination	Temp. (K)	IS (mm/s)	QS (mm/s)	H_F (KOe)	Exp. assignment
Fe^{2+},Ca(1)	6,unrelaxed	0.0	1.11	-4.78	-553	
		300		-1.13		
	6,relaxed[a]	0.0	0.96	4.42	-266	$D1$
		300		1.23		
	5	0.0	0.84	-3.24	-485	
		300		-1.14		
	4	0.0	0.81	-3.73	-534	
		300		-0.98		
Fe^{2+},Ca(2)	6,unrelaxed	0.0	1.18	-2.68	-304	
		300		-1.02		
	6,relaxed[a]	0.0	1.02	-2.23	-481	$D2$
		300		-1.96		
	5	0.0	0.86	-1.93	-460	
		300		-1.17		
	4	0.0	0.99	2.65	-287	
		300		1.04		

[a]Minimum energy configuration at Ca(1),(2) sites according to atomistic simulations.

TABLE X. Calculated Mössbauer isomer shift, quadrupole splitting QS(T), and hyperfine magnetic field $H_F = H_c + H_D$ (see text) of Fe^{3+}-defected HAP. Temperatures of 0 and 300 K are presented.

Ion/site	Coordination	Temp. (K)	IS (mm/s)	QS (mm/s)	H_F (KOe)	Exp. assignment
Fe^{3+},Ca(1)	6,unrelaxed	0.0	0.69	−2.54	−550	
		300		0.40		
	6,relaxed	0.0	0.40	0.22	−487	
		300		0.22		
	5	0.0	0.28	−0.21	−496	
		300		−0.21		
	4 [a]	0.0	0.28	0.84	−484	D4
		300		0.87		
Fe^{3+},Ca(2)	5,unrelaxed	0.0	0.69	1.32	−399	
		300		−0.88		
	6,relaxed	0.0	0.52	1.64	−404	D3
		300		1.28		
	5[a]	0.0	0.30	0.73	−418	
		300		−0.54		
	4	0.0	0.31	1.46	−516	D4
		300		1.04		

[a]Minimum energy configuration at Ca(1),(2) sites according to atomistic simulations.

tion, and related effects on the MB spectra, we investigated the Fe 3d valence partial density of states (PDOS) for both sites, in all geometries. An overview of these PDOS, at the two most stable geometries, is shown in Fig. 7; where the exchange splitting between majority spin (up) and minority spin (down) bands of ~3 eV is evident. The occupied Fe 3d region of a fourfold Ca(1) site displays a greater broadening of the profile than that of a sixfold Ca(2) site, consistent with its lower symmetry and coordination number. Examination of the PDOS at higher resolution permits detailed interpreta-

tion of the level structure, with individual contributions of the $M_L = -2, -1, 0, 1, 2$ subbands to the T dependent QS.

The orbital character and level splittings of the Fe 3d configuration are critical to interpretation of QS and its temperature dependence. In the case of Fe^{3+} one might expect that the half-filled d^5 spin-up shell would be spherical and thus that the QS would be zero. However, the observed nonzero QS demonstrates that anisotropic M_L polarization by ligand bonding interactions is significant. For divalent Fe, we have the additional contributions of ~1 additional, minority
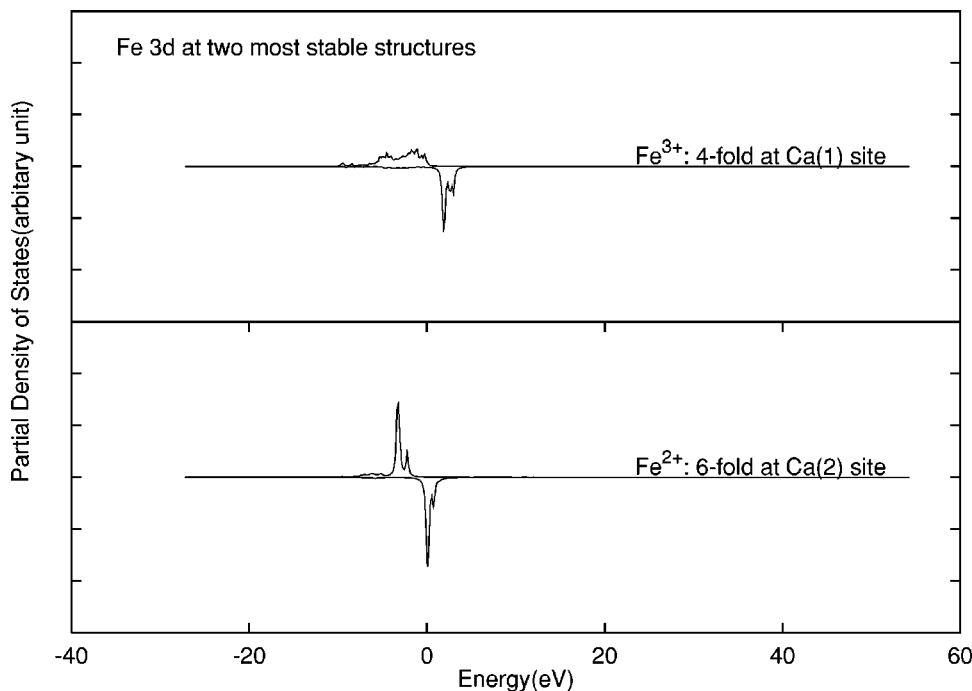

FIG. 7. Partial densities of states (PDOS) for Fe 3d at the two most stable structures. (a) Fe^{2+} sixfold at Ca(2) site and (b) Fe^{3+} fourfold at Ca(1) site. The zero of the energy scale is set at the Fermi energy.

spin, d electron whose orbital composition depends upon local coordination and bonding. The presence of low-lying "crystal field" states of significant Fe $3d$ character also implies their significant occupation at elevated temperatures and consequent effects on QS. In the case of FeHAP we find that the Fe-$3d$ level structure is highly sensitive not only to geometry, but also to the quality of potential representation in the calculations. The observation of QS variations of the order of 25% from $T=4.2$ to 300 K implies the existence of d-character excited states within a few times 0.01 eV of the ground state level. We do indeed find such a level distribution; however, it is not possible to guarantee such high precision, taking into account SCF computational limitations, the approximate nature of lattice relaxations calculated by atomistic simulations, etc. For example, if the SCF procedure is carried out at finite effective temperature, say 300 K, using the appropriate Fermi-Dirac distribution function, the repopulation of M_L character of the $3d$ levels leads in turn to changes in the level structure compared to 0 or 1000 K. Thus a simple Maxwell-Boltzmann population scheme assuming rigid level structure is inappropriate, and physically significant dynamic effects are expected.

With these reservations in mind, we nevertheless find it useful to examine the $T=300$ K SCF level structure for several unrelaxed and relaxed geometries, since they permit semiquantitative predictions consistent with experiment. The predicted T dependence of QS is based upon population of the SCF energy levels (calculated at 300 K), according to the Fermi-Dirac distribution at different T. A more rigorous calculation, wherein the SCF levels would be recalculated for each site at each temperature, is difficult to achieve, due to SCF convergence difficulties for certain sites at very low T.

A detailed analysis would require presentation of partial DOS for both Fe valence states, and for Ca(1)/Ca(2) unrelaxed and relaxed sites in fourfold, fivefold and sixfold ligand coordination. Here we cite the most important features of the critical sites and coordinations.

(1) Fe^{2+} at the unrelaxed Ca(1) site. The lowest lying $3d$-down level is a $M_L=0$ singlet, followed (~0.02 eV) by a $M=\pm2$ doublet and finally by (0.25, 0.35 eV) $M=\pm1$ structure. In perfect C_3 symmetry one would see a singlet and two doublets, with $|M_L|$ degeneracy, as assumed by Ok.[7] However, contrary to the assumptions of Ok, we find that bonding effects place the $M=0$ level lowest, and not $|M|=2$; such level inversions are very commonly seen in ligand-field interactions.

(2) Fe^{2+} at a relaxed Ca(1) site in sixfold coordination. Here the $M=0$ level remains the ground state, but due to the broken C_3 symmetry, the $|M|=2$ degeneracy is lifted, one component becoming almost coincident with $M=0$, the other moving up to ~0.2 eV. The $|M|=1$ levels are also perturbed, moving up to 0.35 ($M=+1$) and 0.75 ($M=-1$) eV. The predicted minimum-energy relaxed geometry thus has a major effect on the level structure and angular character of the minority spin Fe $3d$ levels, with resulting consequences for the QS. It is important to note that the overall d populations are not much changed by relaxation.

(3) Fe^{2+} at the unrelaxed Ca(2) site. Here we find two $3d$ down subbands—the lowest, which is pinned at E_f

has strongly mixed $M=(+2,+1,0,-1)$ character as might be expected from the low site symmetry, and the second, with excitation energy of ~0.4 eV consisting mostly of $M=(-2,0)$ components.

(4) Fe^{2+} at relaxed Ca(2) site in sixfold coordination. Relaxation splits the two bands into three; the lowest-lying containing $M=(+2,+1)$ and a lesser amount of $M=0$, the second at ~0.2 eV with $M=(-1)$, and the third at ~0.75 eV with predominant $M=(-2,0)$ character. The larger spacing of the excited states implies a much reduced variation of QS with T for this site, compared to Ca(1).

(5) Fe^{3+} at the unrelaxed Ca(1) site. Since the $3d$ down band is in principle unoccupied, the predicted $T=0$ QS is due to anisotropic bonding distortions of the deep-lying (~-3 eV) $3d$ up band. However, the excited spin down levels lie very close of E_f and their occupation at finite T would affect QS significantly. This unoccupied $3d$ level structure has approximate composition $M=0$ at $+0.01$ eV, $M=(+2,-2)$ at ~0.03 eV, $M=+1$ at 0.25 eV, and $M=-1$ at 0.35 eV.

(6) Fe^{3+} at relaxed Ca(1) site in fourfold coordination. This energy-favored geometry splits the $3d$-down band into five distinct components, all of which are pushed to considerably higher energy, where they will hardly affect QS T dependence. The lowest band, at ~1.8 eV has mostly $M=-2$ character.

(7) Fe^{3+} at unrelaxed Ca(2) site. Again, four subbands are predicted in this unrelaxed, but low symmetry environment with the lowest, of $M=+2$ character being found just above E_f. The second band, at ~0.05 eV of $M=(+1,-1)$ character would also have noticeable effects on the T-dependent QS.

(8) Fe^{3+} at relaxed Ca(2) site in fourfold coordination. This energy-favored low symmetry arrangement leads to five distinct $3d$-down subbands, two of which can significantly affect QS(T). The lowest, just above E_f, is of $M=+2$ character, while the second, at ~0.02 eV, is of $M=(+1,0)$ character. The remaining band components extend up to ~1.4 eV.

Based upon the site energetics and geometry found from atomistic simulations, and upon the analysis of resulting electronic energy levels and wavefunctions as sketched above, we have made assignments of the four bulk sites observed in MB experiments. It is clear that other assignments may be possible; for example, the x-ray studies of Hughes *et al.*[26] suggest that iron doping may lead to six distinct Ca(2) sites, which is certainly beyond any predictive capabilities at present. However, the general semiquantitative agreement between the present theory and experiment suggests that we have a good starting point for more exact future models.

It would be also very useful to obtain confirming experimental data on the predominant site geometry via spatially resolved spectroscopy such as Fe K-edge x-ray absorption near edge spectroscopy (XANES). To provide a theoretical basis for interpretation of future XANES data, we have calculated approximately the Fe K-edge absorption profile. In the approximation that the $1s\rightarrow4p$ band oscillator strength is only weakly dependent on energy, the XANES profile can be represented by the Fe $4p$ partial density of states. In order
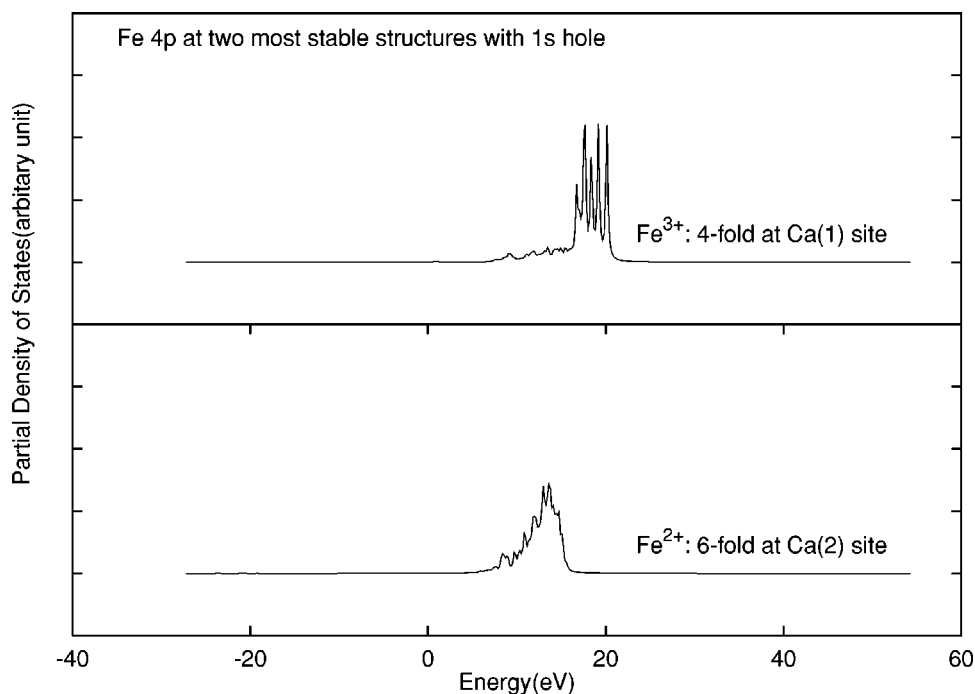
FIG. 8. Fe $4p$ PDOS at the two most stable geometries, calculated in the Fe $1s$ hole-state potential. (a)Fe^{2+} sixfold at Ca(2) site and (b) Fe^{3+} fourfold at Ca(1) site. The zero of the energy scale is set at the Fermi energy.

to consider relaxation effects, we have calculated these profiles in the potential of the cluster with a hole in the Fe^{2+}/Fe^{3+} $1s$ state. Those profiles of Fe^{2+} sixfold at the Ca(2) site and Fe^{3+} fourfold at the Ca(1) site are shown in Fig. 8. The fourfold coordination structure displays a greater broadening of the profiles than sixfold coordination, consistent with the crystal field symmetry around the substituent Fe^{2+}/Fe^{3+} ions. It should be possible to identify the Fe symmetry and coordination number by comparison of our theoretical profiles and experimental XANES if a single site predominates for low concentrations. However, the MB data suggest that a more complex deconvolution of overlapping x-ray spectral features will be necessary.

V. SUMMARY AND CONCLUSIONS

Electron paramagnetic resonance, Mössbauer spectroscopy and electronic structure calculations were combined in order to study the local geometry of Fe^{2+}/Fe^{3+} in Fe-doped hydroxyapatite. The EPR spectrum of FeHAP shows that the isolated high-spin Fe^{3+} ions are at highly distorted octahedral and/or tetrahedral sites of hydroxyapatite, in a strong crystal-field environment. A broad line is also seen, which can be associated with superparamagetic fine particles on the HAP surface.

Atomistic simulations were employed to study relaxation of the HAP lattice around Fe^{2+} and Fe^{3+} substituents at Ca(1) and Ca(2) sites. Fourfold, fivefold and sixfold oxygen coordination was considered, in view of the bonding properties of Fe^{2+}/Fe^{3+} ions in compounds. Considering charge compensation requirements, a defected nonstoichiometric

HAP model was used for Fe^{3+} substitution. Using a minimal Lennard-Jones parametrization of Fe-O interactions, we find that the Ca(2) site is energetically favored over Ca(1) sites for Fe^{2+} substitution and that sixfold coordination is most stable. However for nonstoichiometric Fe^{3+} substitution, the fourfold case is most stable at the Ca(1) site.

Embedded cluster calculations for the relaxed geometries reveal the effective atomic configurations: an Fe^{2+} ion stays in its ideal divalent state in all cases, while an Fe^{3+} ion has $0.5-0.7e$ deviation from the nominal trivalent state due to onset of covalent charge sharing. The two valence states of iron in HAP and defected-HAP have Mössbauer isomer shifts, quadrupole splittings and hyperfine magnetic field which display considerable variation with site geometry and coordination. Comparison of experimental and calculated Mössbauer parameters allows us to conclude that relaxed sixfold Ca(1) and Ca(2) sites are those observed in Fe^{2+}, while Fe^{3+} substitutions result primarily in fourfold sites. Finally, Fe K-edge x-ray absorption profiles were calculated for comparison with future experiments.

[1] L.L. Hench, J. Am. Ceram. Soc. **81**, 1705 (1998); *Biomaterials Science*, edited by B.D. Ratner *et al.* (Academic Press, San Diego, 1996).

[2] Y. Matsumura and J.B. Moffat, Chem. Soc. Faraday Trans. **92**, 1981 (1996).

[3] D.U. Schramm, J. Terra, A.M. Rossi, and D.E. Ellis, Phys. Rev. B **63**, 024107 (2000).

[4] J. Terra, M. Jiang, and D.E. Ellis, Philos. Mag. A **82**, 2357 (2002).

[5] E. Bauminger, S. Ofer, I. Gedalia, G. Horowitz, and I. Mayer, Calcif. Tissue Int. **37**, 386 (1985).

[6] I. Mayer, H. Diab, and I. Felner, J. Inorg. Biochem. **45**, 129 (1992).

[7] Hang Nam Ok, Phys. Rev. **185**, 477 (1969).

[8] B.O. Khudolozhkin, V.S. Urusov, and V.V. Kurash, Geokhimiya **7**, 1081 (1974).

[9] A. Nounah, J. Szilagi, and J.L. Lacoult, Ann. Chim. (Paris) **15**, 409 (1990).

[10] J.D. Gale, J. Chem. Soc., Faraday Trans. **93**, 629 (1997).

[11] K.C. Mundim and D.E. Ellis, Braz. J. Phys. **29**, 199 (1999).

[12] D.E. Ellis and G.S. Painter, Phys. Rev. B **2**, 2887 (1970).

[13] D.E. Ellis and D. Guenzburger, Adv. Quantum Chem. **34**, 51 (1999).

[14] N.N. Greenwood and R.C. Gibb, *Mössbauer Spectroscopy* (Chapman and Hall, London, 1971).

[15] S.H. Vosko, L. Wilk, and M. Nusair, Can. J. Phys. **58**, 1200 (1980).

[16] M. Jiang, Xu-yan Zhou, Bao-xing Li, and Pei-lin Cao, Phys. Rev. B **60**, 8171 (1999).

[17] J. Terra and D.E. Ellis, Phys. Rev. B **56**, 1834 (1997).

[18] P. Dufek, P. Blaha, and K. Schwarz, Phys. Rev. Lett. **75**, 3545 (1995).

[19] A.S. Posner, A. Perloff, and A.F. Diorio, Acta Crystallogr. **11**, 308 (1958).

[20] L.A. Vanina, D.W. Laurent, and D. Mireille, Quant. Chem. **77**, 991 (2000).

[21] A. Chartier, C. Meis, and J.D. Gale, Phys. Rev. B **64**, 085111 (2001).

[22] C. Meis, J.D. Gale, L. Boyer, J. Carpena, and D. Gosset, J. Phys. Chem. A **104**, 5380 (2000).

[23] B.W.H. van Beest, G.J. Kramer, and R.A. van Santen, Phys. Rev. Lett. **64**, 1955 (1990).

[24] G.J. Kramer, A.J.M. de Man, and R.A. van Santen, J. Am. Chem. Soc. **113**, 6435 (1991).

[25] R.F.S. Hearmon, Adv. Phys. **5**, 323 (1956).

[26] J.M. Hughes, A.M. Fransolet, and W. Schreyer, Neues Jahrb. Mineral., Monatsh. **11**, 504 (1993).

[27] A.M. Fransolet and W. Schreyer, Neues Jahrb. Mineral., Monatsh. **7**, 317 (1981).

[28] F. Bodker and S. Morup, Europhys. Lett. **52**, 217 (2000).

[29] T.Jr. Caster, G.S. Newell, W.C. Holton, and C.P. Slichter, J. Chem. Phys. **32**, 3 (1960).

[30] D.L. Griscom, J. Non-Cryst. Solids **40**, 211 (1980).

[31] E.M. Yahiaoui, R. Berger, Y. Servant, J. Kliava, L. Cugunov, and A. Mednis, J. Phys.: Condens. Matter **6**, 9415 (1994).

[32] S. Rossano, E. Balan, G. Morin, J.P. Bauer, G. Calas, and C. Brouder, Phys. Chem. Miner. **26**, 530 (1999).

[33] C.A. dos Santos, A.M.C. Horbe, C.M.O. Barcellos, and J.B. Marimon da Cunha, Solid State Commun. **118**, 449 (2001).